ASME Journal of Fluids Engineering
Online journal at:
https://asmedigitalcollection.asme.org/fluidsengineering

Orientational Dynamics of Long Flexible Fibers in Wall-Bounded Turbulence

Darish Jeswin Dhas
Department of Engineering and Architecture,
University of Udine,
Udine 33100, Italy
e-mail: darishjeswindhas.sam@uniud.it

Cristian Marchioli[1]
Department of Engineering and Architecture,
University of Udine,
Udine 33100, Italy
e-mail: cristian.marchioli@uniud.it

In this paper, we study numerically the role of fiber length and flexibility on the orientational dynamics of slender fibers in turbulent channel flow. We consider fibers of different flexibility at varying aspect ratio, up to lengths being comparable to the channel height. These fibers are constructed by constraining a large number of sub-Kolmogorov rods in a single chain, alongside a bending stiffness torque that allows to prescribe a finite value of the fiber rigidity. To perform our analysis, we carried out a series of one-way coupled direct numerical simulations of a fiber-laden channel flow at fixed shear Reynolds number: $Re_\tau = 300$, based on the half height of the channel. By calculating the orientational statistics of the suspended fibers, we find that shorter fibers, with length $\mathcal{O}(10^{-1})$ when normalized by the channel half height, tend to exhibit a nearly-isotropic orientation distribution near the channel center, as would fibers suspended in homogeneous isotropic turbulence. As the fiber length is increased (up to values comparable to the channel half height), however, deviations from the isotropic orientation distribution become more and more significant. When the fibers are more rigid, these deviations are dampened and it is also observed that the tumbling rate of the fiber is lowered on average. [DOI: 10.1115/1.4068129]

1 Introduction

The problem of a turbulent suspension of long, slender fibers has wide-ranging applications in both industrial and natural settings [1]. Some intriguing applications include drag reduction in oil pipelines, paper and pulp production, ice particles in clouds and microplastics in the ocean and atmosphere. In the current study, we are interested in studying flexible fibers reminiscent of what can be seen in the context of fibrous microplastics that are found in abundance in our oceans and other water bodies [2,3]. Specifically, we focus on the role of fiber length and flexibility in the orientation dynamics of the fibers suspended in wall turbulence. A notable feature of flexible fiber-laden turbulent flows is the complex orientations and interactions between the fibers, and a background turbulent flow offers rich dynamics that profoundly impact the system's collective dynamics. Attempts toward studying the dynamics of slender fibers can be traced back to the theoretical work by Jeffrey back in 1922 [4]. Jeffery's pioneering work gave the expression describing the orbit, now popularly known as Jeffery orbits, executed but ellipsoids suspended in a viscous simple shear flow devoid of fluid inertia. Since then, several studies in the literature have extended this by accounting for additional physics, such as the fiber curvature and inertia [5], and incorporating the effects of fluid inertial forces and torques [6–11]. However, efforts toward studying long flexible fibers suspended in turbulent flows (with lengths many times larger than the Kolmogorov length scale) largely remain a challenge with no possibility of an analytic solution and huge computational costs involved when solving for large swarms of fibers laden in turbulent channel flows.

Several numerical studies in the literature have extensively studied the kinematics and orientational dynamics of rigid fibers suspended in turbulent channel flows [12–18]. In the context of flexible fibers, especially in the context of long fibers, a large body of work exists in the context of fibers suspended in homogeneous isotropic turbulence (HIT) [19,20]. Flexible fibers in HIT have been shown to be capable of being used to measure two-point statistics of turbulence since the suspended fibers tend to flap at a frequency equal to the frequency of the background turbulence [21–24]. In the case of flexible fibers in turbulent channel flow, the numerical investigations in literature have predominantly focused on studying the deformation and orientational dynamics of fibers that are significantly shorter than channel dimensions [25–28]. However, to capture the rich deformation dynamics that flexible fibers can experience in turbulent flows, it is important for the fibers to be sufficiently long, as indicated by the experiments by Brouzet et al. [29]. A recent work by Bec et al. [30] has studied flexible fibers over a wide range of lengths spanning from short to fibers whose lengths are comparable to the channel height of a turbulent channel flow. They use the over-damped slender-body theory to describe the fibers and perform one-way coupled direct numerical simulations with $Re_\tau = 180$. Their simulations showcased how flexible fibers, via near-wall tumbling events, experience enhanced transportation away from the wall. However, while accounting for fiber flexibility, they posit that fiber length and flexibility are directly tied. However, can fiber length and flexibility independently affect their collective dynamics in a turbulent channel flow? The present work stands out by studying fibers of varying lengths and flexibility.

We consider a sparse dispersion of fibers with low volume fractions, $\sim \mathcal{O}(10^{-4})$, which allow us to neglect any feedback of the suspended fibers on the fluid phase and perform one-way coupled simulations. The fibers are assumed to have densities of the same order of magnitude as the suspending fluid, with the density ratio between the fibers and the fluid being fixed as 3. The fibers are

[1]Corresponding author.

Contributed by the Fluids Engineering Division of ASME for publication in the Journal of Fluids Engineering. Manuscript received November 15, 2024; final manuscript received February 21, 2025; published online March 28, 2025. Assoc. Editor: Francesco Zonta.

constructed by connecting point-wise ellipsoids using the rod-chain model and with a bending stiffness torque that allows us to prescribe a degree of rigidity to them [25,31]. The introduction of rigidity allows us to closely approximate physical fibrous suspension, albeit with smaller values of Young's Modulus in our simulations. We then suspend these fibers in a turbulent channel flow possessing a shear Reynolds number of 300 and perform Euler–Lagrange direct numerical simulations of the system. By analyzing the orientational dynamics of the fibers, we find that shorter fibers located near the center tend to orient themselves isotropically of the channel, as expected. However, increasing fiber lengths leads to a progressive deviation from an isotropic distribution of orientation. We also find that the fibers closer to the wall tend to experience higher tumbling rates than the ones closer to the channel center. Further, longer fibers yielded higher tumbling rates, whereas the introduction of rigidity tends to have the opposite effect.

This paper is organized as follows: The description of the problem and the governing system of equations is discussed in Sec. 2. The numerical methodology employed to solve the system of equations described in Sec. 2 is elucidated in Sec. 3. We then discuss the results obtained from the simulations in Sec. 4. Here, we specifically analyze the fibers' average orientation and tumbling and spinning rates. Finally, we draw conclusions based on our findings in Sec. 5.

2 Problem Formulation

We consider long, slender, flexible fibers suspended in a turbulent channel flow. We assume the suspending fibers can be constructed by connecting a series of small ellipsoids, each smaller than the smallest relevant length scale in the flow, the Kolmogorov length scale. This assumption allows for the individual ellipsoids to be modeled as point particles whose translation and rotation dynamics can then be calculated by a force and momentum balance equation system [4,6]. Exploiting the correlation given by Cox [32], these ellipsoids of radius a_{ell} and aspect ratio λ can be mapped to rods of an equivalent radius given as $a = 1.24 a_{\text{ell}}/\sqrt{\ln(\lambda)}$. These rod elements are then connected by placing constraints at their endpoints to form fibers using the rod-chain model as prescribed by Andric et al. [25]. We subsequently describe the dynamics of each point-wise rod elements that make up the fibers using the system of equations describing the position ($\boldsymbol{p}_n$), orientation ($\boldsymbol{o}_n$), linear velocity ($\boldsymbol{v}_n$), and angular velocity ($\boldsymbol{\omega}_n$) of each rod as [28,31]

$$m_n \frac{d\boldsymbol{v}_n}{dt} = \boldsymbol{F}_n^D + \boldsymbol{X}_{n+1} - \boldsymbol{X}_n \tag{1}$$

$$\frac{d\bar{\boldsymbol{J}}\boldsymbol{\omega}_n}{dt} = \boldsymbol{T}_n^D + \boldsymbol{H}_n^D + l\boldsymbol{o}_n \times (\boldsymbol{X}_{n+1} + \boldsymbol{X}_n) + (\boldsymbol{Y}_{n+1,b} - \boldsymbol{Y}_{n,b}) \tag{2}$$

$$\frac{d\boldsymbol{p}_n}{dt} = \boldsymbol{v}_n \tag{3}$$

$$\frac{d\boldsymbol{o}_n}{dt} = \boldsymbol{\omega}_n \times \boldsymbol{o}_n \tag{4}$$

where

$$\bar{\boldsymbol{J}} = \frac{m_n a^2}{12}\left[(4\lambda^2+3)\left(\boldsymbol{I} - \boldsymbol{o}_n\boldsymbol{o}_n^T\right) + 6\boldsymbol{o}_n\boldsymbol{o}_n^T\right] \tag{5}$$

is the inertia tensor of the rod element in the absolute frame of reference, $\boldsymbol{F}_n^D$ is the drag force exerted by the fluid on the rod, $\boldsymbol{T}_n^D$ is the hydrodynamic torque due to the relative spin between fluid and rod, and $\boldsymbol{H}_n^D$ is the hydrodynamic torque due to the fluid velocity gradients' action of the rod. Since each rod element is shorter than the Kolmogorov length scale, it is reasonable to make use of expressions obtained under the framework of Stokes flow theory to describe the aforementioned drag force and hydrodynamic torques. These, in turn, can be written as [33]

$$\boldsymbol{F}_n^D = 6\pi\lambda a\mu\left[Y_n^A\boldsymbol{\delta} + \left(X_n^A - Y_n^A\right)\boldsymbol{o}_n\boldsymbol{o}_n^T\right](\boldsymbol{u}_n - \boldsymbol{v}_n) \tag{6}$$

$$\boldsymbol{T}_n^D = 8\pi\lambda^3a^3\mu\left[Y_n^C\boldsymbol{\delta} + \left(X_n^C - Y_n^C\right)\boldsymbol{o}_n\boldsymbol{o}_n^T\right](\boldsymbol{\Omega}_n - \boldsymbol{\omega}_n) \tag{7}$$

$$\boldsymbol{H}_n^D = -8\pi\lambda^3a^3\mu Y_n^H(\boldsymbol{\epsilon}\boldsymbol{o}_n) : (\dot{\boldsymbol{\gamma}}_n\boldsymbol{o}_n) \tag{8}$$

Here, μ is the viscosity of the suspending fluid; $\boldsymbol{u}_n$, $\boldsymbol{\Omega}_n$, and $\dot{\boldsymbol{\gamma}}_n$ denote the local fluid velocity, rotation, and shear rate at the nth rod element's location; $\boldsymbol{\epsilon}$ is the Levi-Civita third-rank tensor; and X_n^A, Y_n^A, X_n^C, Y_n^C, and Y_n^H are coefficients that depend on the geometric properties of the rod elements given as

$$X_n^A = \frac{8e_{c,n}^3}{-6e_{c,n} + 3\left(1+e_{c,n}^2\right)\log\dfrac{1+e_{c,n}}{1-e_{c,n}}} \tag{9}$$

$$Y_n^A = \frac{16e_{c,n}^3}{6e_{c,n} + 3\left(e_{c,n}^3 - 1\right)\log\dfrac{1+e_{c,n}}{1-e_{c,n}}} \tag{10}$$

$$X_n^C = \frac{4e_{c,n}^3\left(1-e_{c,n}^2\right)}{6e_{c,n} - 3\left(1-e_{c,n}^2\right)\log\dfrac{1+e_{c,n}}{1-e_{c,n}}} \tag{11}$$

$$Y_n^C = \frac{4e_{c,n}^3\left(2-e_{c,n}^2\right)}{-6e_{c,n} - 3\left(1+e_{c,n}^2\right)\log\dfrac{1+e_{c,n}}{1-e_{c,n}}} \tag{12}$$

$$Y_n^H = \frac{4e_{c,n}^5}{-6e_{c,n} + 3\left(1+e_{c,n}^2\right)\log\dfrac{1+e_{c,n}}{1-e_{c,n}}} \tag{13}$$

where $e_{c,n} = \sqrt{(\lambda^2a^2 - a_{ell}^2)/(\lambda^2a^2)}$.

A notable feature of the system of equations we have described is that it allows us to prescribe a bending stiffness to the constructed fibers. We do this by imposing a bending resistance torque given as [31]

$$\boldsymbol{Y}_{n,b} = -\frac{\pi E_Y a^3}{8\lambda}\cos^{-1}(\boldsymbol{o}_n\cdot\boldsymbol{o}_{n-1})\frac{\boldsymbol{o}_n\times\boldsymbol{o}_{n-1}}{|\boldsymbol{o}_n\times\boldsymbol{o}_{n-1}|} \tag{14}$$

where E_Y denotes the Young Modulus of the flexible fiber. Finally, $\boldsymbol{X}$ and $\boldsymbol{Y}$ denote the constraint forces and moments that the connected rod elements exert on each other owing to the no-slip constraint between them, which, in turn, is given by the relation

$$\boldsymbol{p}_n + l\,\boldsymbol{o}_n - (\boldsymbol{p}_{n+1} + l\,\boldsymbol{o}_{n+1}) = 0 \tag{15}$$

With the above system of equations, fibers of different lengths are constructed by simply varying the number of rod elements that make up each flexible fiber.

Having described the suspended fibers, we will describe the fluid flow next. The carrier fluid is considered incompressible and Newtonian, driven by a pressure gradient between two smooth parallel walls of a channel. Typically, the introduction of particulate matter in fluid flows alters the rheological properties, such as the effective density and viscosity of the system, and also exerts additional stresses on the fluid phase [34]. However, although the fibers we are interested in possess densities higher than the suspending fluid, we consider very low-volume fractions $\left(\sim\mathcal{O}(10^{-4})\right)$. Such low-volume fractions of suspensions allow us to neglect any modification to the flow properties by the presence of the fibers using a one-way coupled description of the system. Therefore, we can write down the continuity and momentum balance equations as

$$\nabla \cdot \boldsymbol{u} = 0 \tag{16}$$

$$\rho\left[\frac{\partial \boldsymbol{u}}{\partial t} + \boldsymbol{u}\cdot\nabla \boldsymbol{u}\right] = -\nabla P + \mu \nabla^2 \boldsymbol{u} \tag{17}$$

Here, $\boldsymbol{u} = (u_x, u_y, u_z)$ is the velocity field, P is the pressure field, and ρ is the density of the carrier fluid. The above equations are complemented by the no-slip and no-penetration boundary conditions at both the top and bottom walls as $\boldsymbol{u} = 0$, along with periodic boundary conditions along the streamwise and spanwise extremities. As per convention in wall-bounded turbulent flows, we next make the above system of equations nondimensional in terms of wall units. These are denoted by the superscript "+" hereinafter. We do this by using the viscous length and times scales as $\mu/(\rho u_\tau)$ and $\mu/(\rho u_\tau^2)$ toward nondimensionalizing the equations. Here, the reference velocity u_τ refers to the friction velocity defined as $u_\tau = \sqrt{\tau_w/\rho}$, where τ_w is the shear stress exerted by the flow at the wall. Following this, the angular velocities are made dimensionless as $\boldsymbol{\omega}^+ = \boldsymbol{\omega}\mu/(\rho u_\tau^2)$, fiber's density as $\rho^+ = \rho_p/\rho$ and Young Modulus as $E_Y^+ = E_Y/(\rho u_\tau^2)$. Furthermore, we use the fiber response time defined as in Dotto et al. [27] to obtain the fiber Stokes number as

$$\mathrm{St}_{\mathrm{fiber}} = \frac{2}{9} a^{+^2} \rho^+ \lambda_{\mathrm{tot}} \frac{\log\left(\lambda_{\mathrm{tot}} + \sqrt{\lambda_{\mathrm{tot}}^2 - 1}\right)}{\sqrt{\lambda_{\mathrm{tot}}^2 - 1}} \tag{18}$$

This definition corresponds to that of a rigid fiber in its fully stretched configuration.

3 Numerical Methodology

With the governing system of equations described in Sec. 2, we next proceed to describe the numerical methodology that we employ to solve them. For this, we follow a pseudo-spectral approach, wherein the equations of motions pertaining to the fluid are solved in a modal space on an Eulerian grid. The convective terms in the Navier–Stokes equation $\boldsymbol{u}\cdot\nabla\boldsymbol{u}$ are resolved in the physical space and then transformed [35]. The streamwise and spanwise directions (x and y) are discretized in Fourier space, the advantage of which is the implicit satisfaction of the periodic boundary conditions. The wall-normal coordinate (z) is discredited using Chebyshev polynomials. Time advancement is treated using an implicit-explicit scheme, using a combination of an explicit Adam-Bashforth scheme and implicit second-order Crank-Nicolson.

To solve for the dynamics of the fibers, we first interpolate the flow velocities and velocity gradients and evaluate them at the location of the point-wise rod elements using 4th-order polynomials. While we do not account for fiber–fiber interactions owing to our small volume fractions, the fiber–wall interactions are modeled considering purely elastic collisions. This implies that when a rod element comes into contact with a wall, it will be bounced back according to the position of the rod element that is closest to the wall. This numerical methodology is implemented via a bespoke in-house graphics processing unit (GPU)-accelerated solver named surf_gpu. We refer interested readers to Di Giusto and Marchioli [28] for further details on the flow solver employed for the current work.

The simulations reported in this paper are performed for a fiber-laden turbulent channel flow with a shear Reynolds number Re_τ of 300. The channel dimensions are $L_x \times L_y \times L_z = 4\pi h \times 2\pi h \times 2h$ in physical units, which corresponds to a flow of water at bulk velocity $u_b = 0.3\,\mathrm{m/s}$ in a channel of size $0.25 \times 0.13 \times 0.04\,\mathrm{m}^3$. When written in wall units, the channel dimensions can be expressed as $4\pi\mathrm{Re}_\tau \times 2\pi\mathrm{Re}_\tau \times 2\mathrm{Re}_\tau$. This domain is solved using a $512 \times 256 \times 129$ grid. Each suspended rod element is assumed to have a fixed aspect ratio $\lambda = 5$. Subsequently, flexible fibers of differing lengths are constructed by varying the number of rods that are connected together to make up each flexible fiber, with L_0^+ denoting their fully stretched length. The total aspect ratio of the resulting fibers, therefore, becomes $\lambda_{\mathrm{tot}} = \lambda\, n_{\mathrm{rods}}$, where n_{rods} denotes the number of rods that make up each fiber. We fix the radius of the rod elements to be $a^+ \approx 0.16$ and the density to be $\rho^+ = 3$.[2] This, in turn, yields a Stokes number of $\mathrm{St}_{\mathrm{fiber}} \approx 0.1$ for all the cases explored. Note that, in our simulations, the Froude number for the fibers, defined as $\mathrm{Fr} = u_b/(\tau_p g)$ with τ_p the fiber's relaxation time and g the acceleration due to gravity, is $\gg 1$ (more specifically, $\mathcal{O}(10^2)$ for the aforementioned physical system). This allows us to neglect any potential effects of gravity on the fibers' dynamics. We also fix the total number of rod elements in all our simulations to 1.2×10^6. This makes the total volume fraction of the fibers in the channel flow to be 1.064×10^{-4}. As indicated by the governing equations in Sec. 2, the simulations are one-way coupled.

Table 1 Parametric combinations considered

Case no.	E_Y^+	λ_{tot}	L_0^+	L_0^+/Re_τ
1	0	100	33.65	0.11
2	10^5	100	33.65	0.11
3	0	200	66.38	0.22
4	10^5	200	66.38	0.22
5	0	400	131.27	0.44
6	10^5	400	131.27	0.44
7	0	800	260.12	0.87
8	10^5	800	260.12	0.87

4 Simulation Results

Using the numerical methodology described in Sec. 3, we next proceed to perform a set of direct numerical simulations. With the specific intent to study the role of fiber length and flexibility, we choose a range of parameters for our simulations comprising combinations of four values of aspect ratios/fiber lengths and two Young's Modulus. The details pertaining to each simulation case considered are tabulated in Table 1. As indicated in the table, we explore fibers whose lengths vary from being an order of magnitude smaller than the half-channel height to being comparable to the half-channel height.

All statistics reported in this section are sampled every 15 t^+. Convergence of statistics is ensured by performing all the simulations up to 3000 t^+ and then choosing the averaging window to be between 1500 and 3000 t^+. This is sufficient as the averaging window corresponds to four times the eddy turnover time of the largest turbulence structures. Figure 1 shows snapshots of the fiber distribution of the shortest and longest fibers simulated with $E_Y^+ = 10^5$. For better visualization, we choose to show a random selection of 1000 short fibers and 200 long fibers in Figs. 1(*a*) and 1(*b*), respectively. Further, the fiber thickness is exaggerated and not true to size for the same purpose. It is clear from the images how, despite the equal rigidity, the longer fibers tend to undergo significant deformations exhibiting complex shapes compared to the short fibers.

We first discuss how we calculate the statistical quantities we are interested in as we move from a "rod element" description of the system we solve for to a fiber-centered description. The position of the fibers in the channel is characterized by their center of mass calculated as

$$\boldsymbol{p}_{\mathrm{cm}} = \frac{\sum_{i=1}^{N} \boldsymbol{p}_i}{N} \tag{19}$$

[2]In the context of marine microplastics, the heaviest commonly-recovered samples happen to be polytetrafluoroethylene, which has a density about 2.2 times larger than water. A further increase of density, up to 1–1.5%, can occur in the case of plastics that undergo biofouling. Hence, a density ratio equal to 3 appears to represent a safe upper boundary for the highest-density marine microplastics.

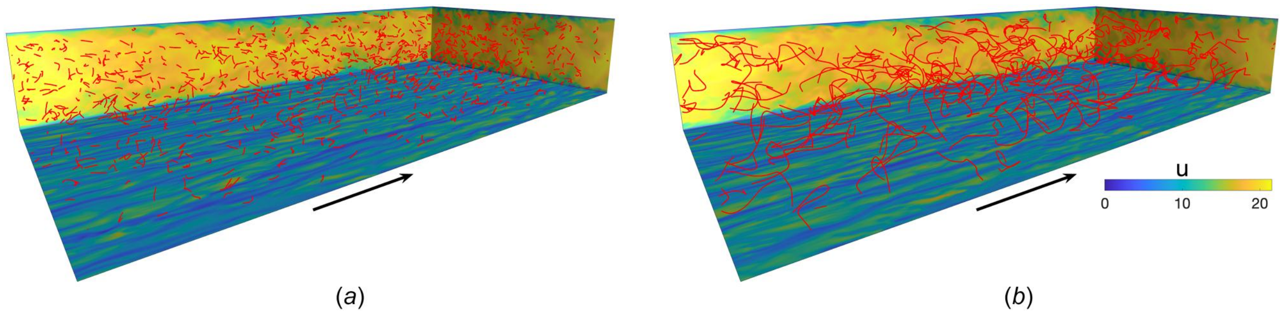

Fig. 1 Instantaneous distribution of a random collection of flexible fibers of length $L_0^+ = 33.65$ (*a*) and $L_0^+ = 260.12$ (*b*) in a turbulent channel flow with $Re_\tau = 300$. The side and bottom panels display the stream-wise component of the velocity, with the bottom cut at $z^+ = 10$. The fiber thickness is magnified for better visualization.

Here, subscripts 1 and N denote the first and last rod element of each fiber, respectively. Similarly, we take linear and angular velocities of the fibers to be the corresponding quantities averaged about the rod elements that make up each fiber. Following Andrić et al. [25], the normalized average orientation of the rod elements is calculated as

$$\boldsymbol{n} = \frac{\sum_{i=1}^{N} \boldsymbol{o}_i}{\left|\sum_{i=1}^{N} \boldsymbol{o}_i\right|} \tag{20}$$

To get a flavor of how the fibers move inside the turbulent channel, we first showcase the evolution of the position of selected fibers as they start their life inside the channel. More importantly, we are interested in showcasing how fibers that start at various locations along the gradient direction evolve in the flow. It is crucial to acknowledge here that observations made by following individual fibers would not necessarily reflect their collective behaviors. Nevertheless, we do this to showcase the transient behavior of fibers from different wall-normal locations in the channel. Figure 2 shows the fibers' position and orientation with respect to the flow direction (x) till time $t^+ = 1200$ for the shortest and longest fibers ($L_0^+ = 33.65$ and 260.12 respectively) we have considered, possessing two values of Young's modulus $E_Y^+ = 0$ and 10^5. Note that time $t^+ = 1200$ is approximately equal to three times the eddy turnover time of the largest structures in the flow. Within this time span, the fibers pass through the box in the streamwise direction multiple times, the exact number of times depending on the length of the fibers and on the region of the flow that they sample (fibers travel much faster in the streamwise direction when they in the channel center, while being much slower near the wall). For the longest fibers considered, the fibers sweep the box in the streamwise direction at least six times within the time frame considered.

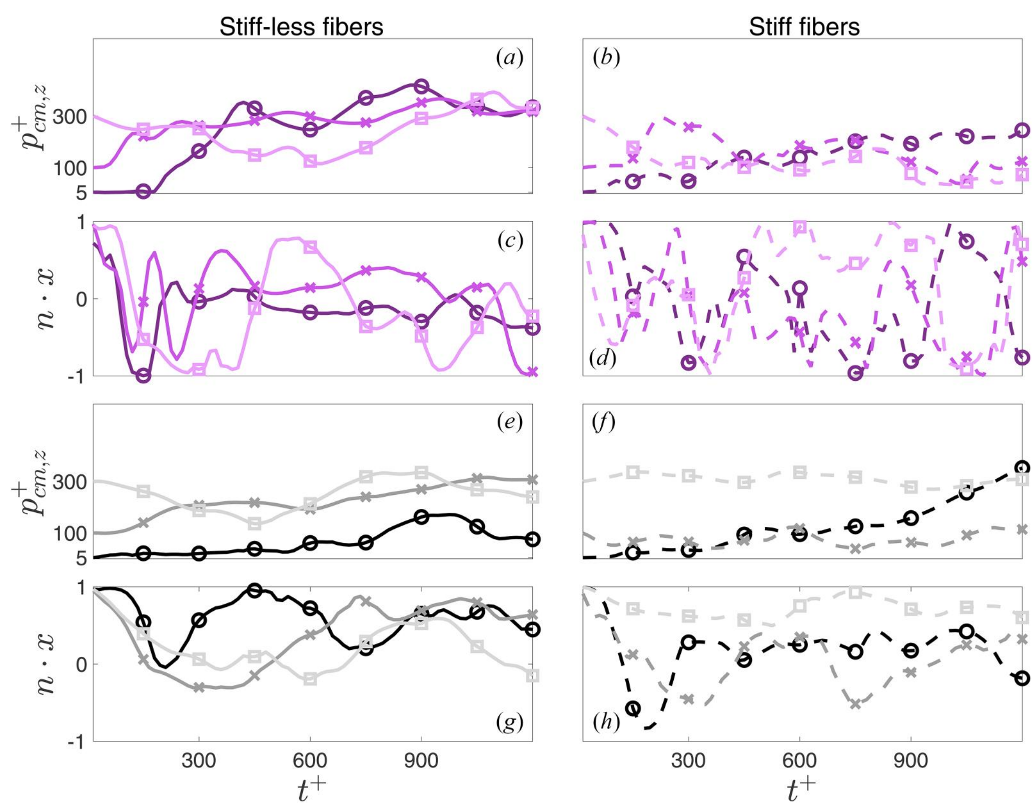

Fig. 2 Time evolution of fibers with $L_0^+ = 33.65$ (———) and $L_0^+ = 260.12$ (———), whose initial wall-normal position begins at $z^+ = 5$, 100, and 300, denoted by "○", "×," and "□," respectively, also indicated by the lighter shades indicating increasing distance from the wall. $E_Y^+ = 0$ (solid lines) and $E_Y^+ = 10^5$ (dash lines).

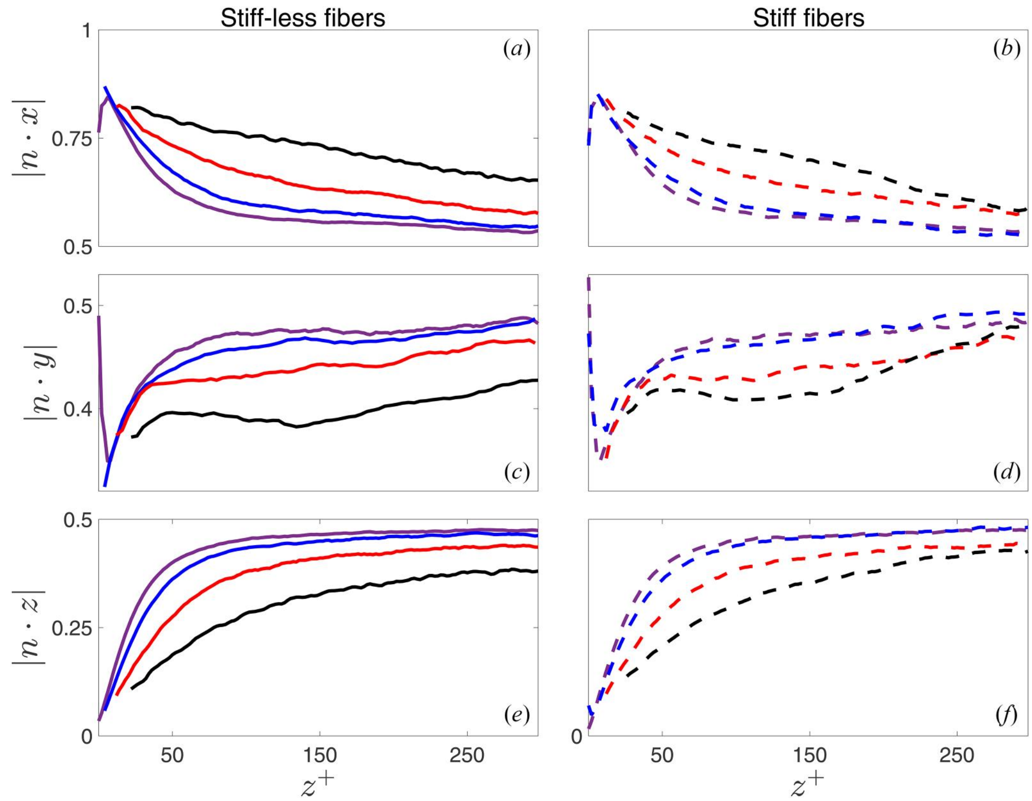

Fig. 3 Components of the orientation vectors of the fibers with lengths $L_0^+ = 33.65$ (——), $L_0^+ = 66.38$ (——), $L_0^+ = 131.27$ (——) and $L_0^+ = 260.12$ (——), and $E_Y^+ = 0$ (solid lines) and $E_Y^+ = 10^5$ (dash lines)

We pick fibers whose center of mass lies at $z^+ = 5$, 100, and 300 to track. This lets us visualize the evolution of a fiber that begins its journey close to the wall, far from the wall and the channel center, respectively. We first focus on the shortest of our fibers (panels a to d in Fig. 2). Looking at the evolution of the center of mass, we find that the short fibers with zero flexural rigidity ($E_Y^+ = 0$) move with a bias toward the center of the channel (away from the wall). However, the bias is lower for the rigid short-fiber case as we do not observe a strong migration. The same can be said for the long fibers ($L_0^+ = 260.12$) irrespective of their rigidity. Focusing on the evolution of the orientation of the fibers, we find that the stiffer fibers tend to reorient more abruptly than their counterparts that possess zero flexural rigidity. As expected, shorter fibers undergo rapid reorientations, especially the ones closer to the wall. The longer fibers, especially the ones with zero flexural rigidity, tend to enjoy extended periods in flow-aligned orientation. However, we observe abrupt reorientations for the rigid, long fibers closer to the wall. Upon closer examination juxtaposing the orientation and position plots, we speculate that their reorientations could be due to the fibers' pole vaulting, resulting in their migration toward the channel center [30,36–39]. Note that, as pointed out previously in literature, the pole vaulting mechanism is reliant on the fibers being sufficiently rigid.

Having looked at the dynamics of individual fibers, the next task is to study the collective dynamics by means of computing statistics that are averaged both spatially and temporally. All the statistics showcased henceforth are computed by averaging across the streamwise and spanwise directions and plotted with respect to the distance of the fibers' center of mass from the wall, and the temporal averaging performed as previously mentioned. Following this approach, we first compute and showcase the averaged orientations of the fibers as calculated from Eq. (20), plotted along the wall-normal direction in Fig. 3. It must be noted that a value of 0.5 in these plots represents an isotropic distribution of orientation. What is immediately noticeable is the apparent impact of varying fiber lengths on their orientational dynamics. It is previously seen in literature that fibers suspended in HIT tend to exhibit an isotropic orientation distribution [1,24,40]. Considering that the region near the center of the channel is reminiscent of HIT, we observe a similar close to an isotropic distribution of orientation amongst the shorter fibers with $L_0^+ = 33.65$ and 66.38 in that region. However, we observe a progressive deviation from this behavior as we transition toward longer fibers with $L_0^+ = 131.27$ and 260.12. This could be because longer fibers have the capability to sample a much larger flow region. This means that although the center of mass of the fibers might lie near the channel center, the extremities might be exposed to flow regions that are potentially closer to the wall.

As we move toward the walls, we no longer observe an isotropic orientation distribution but rather a strong preferential alignment with the streamwise direction irrespective of the fiber length. This, again, is reminiscent of what was previously observed in the case of relatively shorter fibers [1,13] and equally long fibers [30] suspended in wall-bounded flows. Regarding the flexibility/rigidity of the suspended fibers, we find that fiber rigidity tends to dampen the deviations that varying fiber lengths bring to the averaged orientation angles.

Now that we know how the fibers like to align themselves in the flow, we are next interested in how they tumble and spin inside the flow. We calculate the tumbling rate, which measures the rotation of the fiber axis of symmetry here characterized by its mean square value as

$$\langle \dot{\boldsymbol{n}}\, \dot{\boldsymbol{n}} \rangle = |\omega \times \boldsymbol{n}|^2 \tag{21}$$

and the mean square spinning rate that measures the rotation around the fibers' axis of symmetry as $|\boldsymbol{n} \cdot \omega|^2$ [40]. We already know that the orientations of the fibers closer to the center of the channel, henceforth referred to as the "bulk" flow region, closely resemble what was already seen in fibers suspended in HIT. To further test this and make direct comparisons with experiments on HIT, we first plot the probability distribution of the normalized mean square tumbling rate, specifically at the bulk and the near-wall region. We categorize

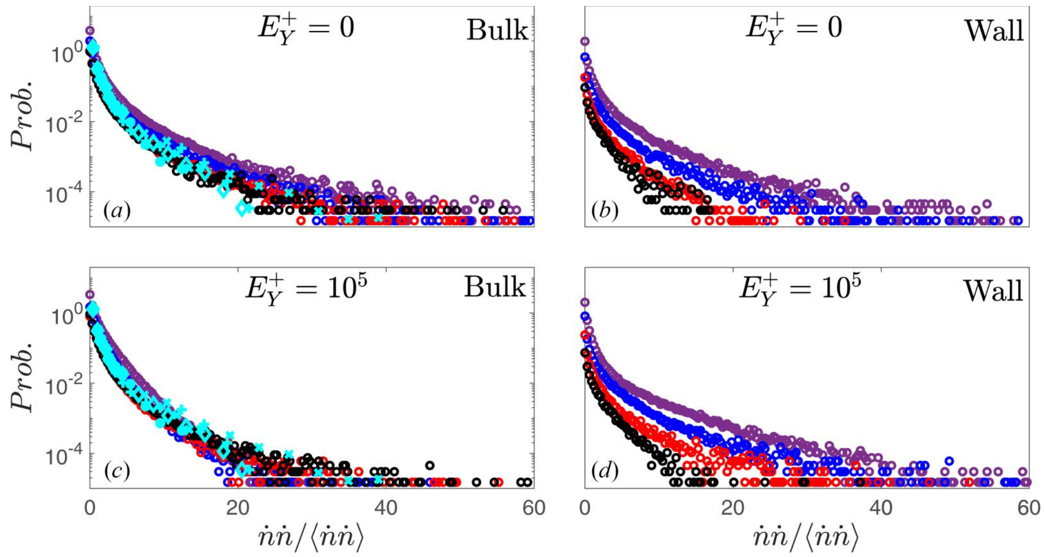

Fig. 4 Probability of the mean square tumbling rate of the fibers with lengths $L_0^+ = 33.65$ (purple line), $L_0^+ = 66.38$ (blue line), $L_0^+ = 131.27$ (red line) and $L_0^+ = 260.12$ (black line). Results from Parsa and Voth [41] are shown in cyan color with fiber lengths $L = 8.5\eta$ ("x"), $L = 32.8\eta$ ("◇"), $L = 42.4\eta$ ("+"), and $L = 72.9\eta$ ("*").

the region that is 30 wall units above and below the half-height of the channel as the bulk region and the region from the wall to 60 wall units as the wall region. For a suitable comparison with the experimental findings, we use the local values of the mean square tumbling rates calculated from the bulk and the near-wall regions to normalize the squared tumbling rates of fibers pertaining to those regions. Figures 4(*a*) and 4(*c*) show these probabilities for the flexible and rigid fibers, respectively. For the flexible fibers, we find a weak influence of the fiber length on the tumbling rate probabilities. This influence becomes even more weaker when considering rigid fibers.

Parsa and Voth [41] experimentally studied the dynamics of nylon threads of varying lengths suspended in HIT. They showcase their fiber lengths normalized with respect to the Kolmogorov length scale. Therefore, we show the fibers' length normalized by the Kolmogorov length scale calculated at the channel center. We then compare the probability distribution obtained from our simulations with that of Parsa and Voth [41], denoted by cyan-colored markers for optimal visibility. For direct comparison with their experiments, it is useful to normalize the fiber length with respect to the Kolmogorov length scale calculated from the channel center. Doing this, the fiber lengths can be rewritten as $L_0^+ = 3.58\eta^+$, $L_0^+ = 7.06\eta^+$, $L_0^+ = 13.97\eta^+$, and $L_0^+ = 27.69\eta^+$. Looking at Fig. 4(*a*), we find that dependence on fiber length is a lot more prominent in our simulations than seen in their experiments. However, the probability distribution of the long flexible fibers agrees with the experimental findings. Making the same comparison with the simulation results of the rigid fibers, we find excellent agreement between the two (see Fig. 4(*c*)). Since nylon threads possess a finite degree of rigidity, the results from rigid fibers find better agreement with the experiments expectantly.

On the other hand, tumbling rates of the fibers in the near-wall region tend to be more sensitive to the fiber length, as is evident from the broader tails seen in probability distribution plotted in Figs. 4(*b*) and 4(*d*). To better understand this, we next plot the dimensionless mean square tumbling rate as a function of the wall-normal coordinate in Figs. 5(*a*) and 5(*b*). The most prominent finding is that fibers near the wall tend to tumble at rates two to three orders of

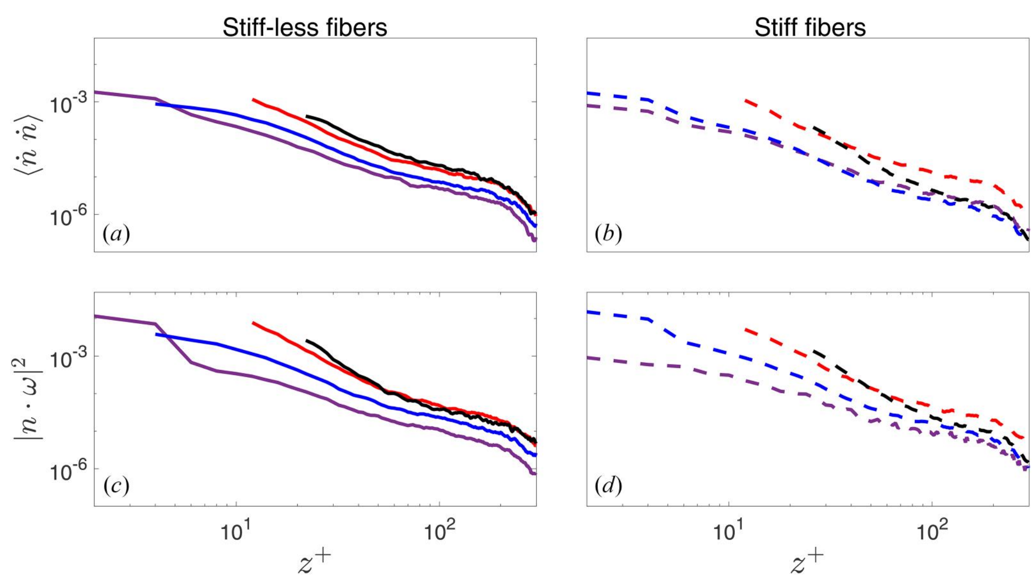

Fig. 5 Mean square tumbling rates (*a* and *b*) and spinning rates (*c* and *d*) of the fibers with lengths $L_0^+ = 33.65$ (purple line), $L_0^+ = 66.38$ (blue line), $L_0^+ = 131.27$ (red line) and $L_0^+ = 260.12$ (black line), and $E_Y^+ = 0$ (solid lines) and $E_Y^+ = 10^5$ (dash lines)

magnitude larger than those near the channel center. Such increased near-wall tumbling rates can be attributed to a combination of increased turbulence fluctuations near the wall [42] and collisions of the fibers with the wall [30]. However, the center of the channel is essentially a quiescent core, yielding significantly lower tumbling rates. These observations are consistent with previous experiments and simulations in literature [1,13,38,43], and hold true for both rigid and flexible fibers. Furthermore, we also find that increasing fiber lengths yield larger tumbling rates. This is due to the long fibers being able to interact with more energetic eddies [43]. To precisely discern the effect of rigidity on tumbling rates, we contrast the flexible and rigid ones corresponding to the same fiber length. By doing this, we can observe a reduction in the mean square tumbling rates in the rigid fibers compared to their flexible counterparts. This reduction is minimal and mostly confined to the near-wall region for the short fibers. However, long rigid fibers see a significant reduction in the mean square tumbling rates compared to flexible fibers of the same length. Finally, we plot the spinning rates of all the cases in Figs. 5(*c*) and 5(*d*). Comparing Figs. 5(*c*) and 5(*d*) with Figs. 5(*a*) and 5(*b*), it is evident that the magnitudes of spinning rates are higher than those of the tumbling rates. This is consistent with the experimental measurements on long fibers suspended in homogeneous isotropic turbulence [20], and on short curved fibers suspended in a turbulent channel flow [42]. Such increased spinning rate magnitudes can be attributed to the fibers being trapped by the elongated vortical structures of the background turbulence [20]. With regard to varying fiber lengths and flexibility, we find that they have a qualitatively similar impact on the spinning rates as they did with the tumbling rates.

5 Discussions and Conclusions

In this paper, we have investigated the orientational dynamics of flexible fibers of varying lengths and flexibility suspended in a turbulent channel flow at shear Reynolds number $\mathrm{Re}_\tau = 300$ by means of Euler–Lagrange simulations. The flexible fibers are modeled by connecting sub-Kolmogorov-sized rod-like elements to form long chains [25]. Additionally, by incorporating a bending resistance torque [31], we have studied both fully flexible and rigid fibers with Young's modulus of $E_Y^+ = 0$ and 10^5, respectively. This formulation allows the study of flexible fibers of length comparable to the half-height of the channel while using relations from Stokes flow theory to prescribe the forces and torques that each rod-like element experiences in the flow.

We first examined the temporal evolution of the fibers from different locations from the wall by tracking the position of their center of mass and orientation vector with respect to the streamwise direction. Our results show that shorter flexible fibers tend to migrate away from the wall, whereas their rigid counterparts stay closer to the wall and experience more rapid changes in orientations. However, the temporal behavior of the longer fibers is found to be less sensitive to their flexibility/rigidity as they move and orient themselves similarly, irrespective of their bending stiffness. Collating the rapid changes in orientation of the fibers closer to the wall and their subsequent journey away from the wall hints at the possibility of the fibers pole-vaulting toward their journey away from the wall, as previously observed in the literature [30,36–39].

To study the fiber orientation based on their location along the channel height, we have next discussed the fiber spatially and temporally averaged orientational vectors. Reminiscent of experimental and numerical observations made on fibers suspended in HIT, we find that short fibers closer to the channel center tend to orient themselves isotropically in the flow. However, we also find that longer fibers tend to progressively deviate from an isotropic distribution with increasing fiber length. This deviation could be due to the capability of longer fibers to sample a more extensive range of flow scales, although their center of mass might lie within the channel center. Although Bec et al. [30] found similar trends with respect to fiber lengths, they reported a smaller magnitude of deviations in comparison to what we observed. This variation can be attributed to the methodology employed in calculating the orientation vectors, wherein they calculated the local orientation of each fiber. In contrast, we calculate the orientation of the fiber as a whole using Eq. (20). We also observe that fiber rigidity tends to minimize the deviations with respect to increasing fiber lengths, especially closer to the channel center.

Finally, we have analyzed the rotation rates of the fibers by calculating their tumbling and spinning rates. We first discussed the probability distribution of the normalized mean square tumbling rates experienced by the fibers closer to the center of the channel and closer to the wall separately. Focusing first on the fibers near the channel center, we find a clear dependence on the rigidity of the fibers on the probability distribution of the tumbling rates. We observe that the fully flexible fibers tend to have fatter tails in the distribution, hinting at dependence on fiber length. However, we also observe that the opposite happens in the case of rigid fibers. By comparing our findings with the experimentally calculated probability distribution of the mean square tumbling rate by Parsa and Voth [41], we find that the experiments best agree with our simulations with rigid fibers. This could be due to the finite rigidity of the nylon fibers used in their experiments. Nylon fibers also possess comparable density with respect to the suspending fluid in their experiments, making comparisons with their findings all the more suitable. It is also worth noting that the experiments by Parsa and Voth [41] were conducted in HIT with a Taylor Reynolds number of 150 and 210. Plotting the tumbling and spinning rates along the channel depth, we can make the following observations. Owing to the strong turbulence fluctuations that occur close to the wall and to fiber-wall collisions, fibers in that region tend to tumble and spin at rates significantly higher than those closer to the channel center. We also find that increasing fiber lengths tend to yield higher tumbling and spinning rates, but increased rigidity has the opposite effect.

A common feature observed in all the statistics along the wall-normal direction is the progressive absence of data closer to the walls of the channel for longer fibers. This is because longer fibers tend to move away from the wall, creating an inhomogeneous particle distribution. Therefore, as shown by Bec et al. [30], this leads to an apparent depletion in the boundary layer that progressively becomes stronger with increasing fiber lengths. Another major takeaway from the current paper is the specific role that the introduction of fiber rigidity brings to the collective dynamics of the fibers. In the introduction, we asked whether fiber length and flexibility can affect their collective dynamics independently. Our results comparing rigid and flexible fibers show that rigidity does indeed play independent roles in modulating the orientation dynamics of the fibers, albeit quantitatively. A future study that covers a broader range of bending stiffness values and fiber lengths is warranted to thoroughly quantify their individual roles in the dynamics of the system.

The main focus of this paper has been to probe the role of fiber length and flexibility, specifically on the orientational dynamics of fibers suspended in a turbulent channel flow. Since the suspended fibers are flexible, a natural next step would be to study how they deform. Studies in the past have looked at the flapping frequencies of flexible fibers suspended in HIT [21,24,44] and also the migration of fully flexible fibers away from the wall as a consequence of the fibers' contact with the channel wall [30]. Therefore, our future efforts will be devoted to the characterization of the flapping and deformation modes as a function of a range of fiber lengths and rigidity, as well as the inertia of the background flow by contrasting the fiber dynamics suspended in turbulent channel flows with different values of shear Reynolds numbers. In the current work, we have focused on fibers that possess negligible inertia, as indicated by the Stokes number and the particle Reynolds number. While such fibers are relevant to marine microplastics, atmospheric microplastics tend to possess larger values of fluid inertia owing to significant density differences. Studying such a system would also entail accounting for the effects of fluid inertia on the calculation of the forces and torques experienced by the suspended fibers [8,45]. Such a study would be another natural extension of the current work, which would be the subject of another future paper.

Acknowledgment

We thankfully acknowledge CINECA for the high-performance computing resources made available to us under the ISCRA initiative.

Data Availability Statement

The datasets generated and supporting the findings of this article are obtainable from the corresponding author upon reasonable request.

Nomenclature

$E_Y =$ fiber Young's modulus (kg m^{-1} s^{-2})
$m_n =$ mass of the nth fiber (kg)
$\boldsymbol{o}_n =$ orientation vector of the nth fiber (rad)
$\boldsymbol{p}_n =$ position vector of the nth fiber (m)
$\mathrm{Re}_\tau =$ Reynolds number, $\rho u_\tau h/\mu$
$\mathrm{St}_{\mathrm{fiber}} =$ Stokes number, $\frac{2}{9} a^{+^2} \rho^+ \lambda_{\mathrm{tot}} \frac{\log\left(\lambda_{\mathrm{tot}}+\sqrt{\lambda_{\mathrm{tot}}^2-1}\right)}{\sqrt{\lambda_{\mathrm{tot}}^2-1}}$
$\boldsymbol{u} =$ velocity vector of the fluid (m s^{-1})
$u_\tau =$ shear velocity (m s^{-1})
$\boldsymbol{v}_n =$ velocity vector of the nth fiber (m s^{-1})
$2a =$ fiber diameter (m)
$2h =$ channel height (m)
$2l =$ fiber length (m)
$\lambda =$ aspect ratio of ellipsoids, l/a
$\lambda_{\mathrm{tot}} =$ total aspect ratio of the fibers, $n_{\mathrm{rods}}\,\lambda$
$\mu =$ dynamic viscosity (kg m^{-1} s^{-1})
$\rho =$ fluid density (kg m^{-3})
$\rho_p =$ fiber density (kg m^{-3})
$\rho^+ =$ density ratio, ρ_p/ρ
$\boldsymbol{\omega}_n =$ angular velocity vector of the nth fiber (s^{-1})
$\boldsymbol{\Omega} =$ angular velocity vector of the fluid (s^{-1})

References

[1] Voth, G. A., and Soldati, A., 2017, "Anisotropic Particles in Turbulence," Annu. Rev. Fluid Mech., **49**(1), pp. 249–276.
[2] Hale, R. C., Seeley, M. E., La Guardia, M. J., Mai, L., and Zeng, E. Y., 2020, "A Global Perspective on Microplastics," J. Geophys. Res.: Oceans, **125**(1), p. e2018JC014719.
[3] Brouzet, C., Guiné, R., Dalbe, M.-J., Favier, B., Vandenberghe, N., Villermaux, E., and Verhille, G., 2021, "Laboratory Model for Plastic Fragmentation in the Turbulent Ocean," Phys. Rev. Fluids, **6**(2), p. 024601.
[4] Jeffery, G. B., 1922, "The Motion of Ellipsoidal Particles Immersed in a Viscous Fluid," Proc. R. Soc. London, Ser. A, **102**(715), pp. 161–179.
[5] Khayat, R., and Cox, R., 1989, "Inertia Effects on the Motion of Long Slender Bodies," J. Fluid Mech., **209**, pp. 435–462.
[6] Brenner, H., and Cox, R., 1963, "The Resistance to a Particle of Arbitrary Shape in Translational Motion at Small Reynolds Numbers," J. Fluid Mech., **17**(4), pp. 561–595.
[7] Subramanian, G., and Koch, D. L., 2005, "Inertial Effects on Fibre Motion in Simple Shear Flow," J. Fluid Mech., **535**, pp. 383–414.
[8] Dabade, V., Marath, N. K., and Subramanian, G., 2015, "Effects of Inertia and Viscoelasticity on Sedimenting Anisotropic Particles," J. Fluid Mech., **778**, pp. 133–188.
[9] Einarsson, J., Candelier, F., Lundell, F., Angilella, J., and Mehlig, B., 2015, "Rotation of a Spheroid in a Simple Shear at Small Reynolds Number," Phys. Fluids, **27**(6), p. 063301.
[10] Marath, N. K., and Subramanian, G., 2018, "The Inertial Orientation Dynamics of Anisotropic Particles in Planar Linear Flows," J. Fluid Mech., **844**, pp. 357–402.
[11] Candelier, F., Mehlig, B., and Magnaudet, J., 2019, "Time-Dependent Lift and Drag on a Rigid Body in a Viscous Steady Linear Flow," J. Fluid Mech., **864**, pp. 554–595.
[12] Paschkewitz, J., Dubief, Y., Dimitropoulos, C. D., Shaqfeh, E. S., and Moin, P., 2004, "Numerical Simulation of Turbulent Drag Reduction Using Rigid Fibres," J. Fluid Mech., **518**, pp. 281–317.
[13] Marchioli, C., Fantoni, M., and Soldati, A., 2010, "Orientation, Distribution, and Deposition of Elongated, Inertial Fibers in Turbulent Channel Flow," Phys. Fluids, **22**(3), p. 033301.
[14] Zhao, L., and Marchioli, C., and Anderson, H. I., 2014, "Slip Velocity of Rigid Fibers in Turbulent Channel Flow," Phys. Fluids, **26**(6), p. 063302.
[15] Marchioli, C., Zhao, L., and Andersson, H., 2016, "On the Relative Rotational Motion Between Rigid Fibers and Fluid in Turbulent Channel Flow," Phys. Fluids, **28**(1), p. 013301.
[16] Shaik, S., Kuperman, S., Rinsky, V., and van Hout, R., 2020, "Measurements of Length Effects on the Dynamics of Rigid Fibers in a Turbulent Channel Flow," Phys. Rev. Fluids, **5**(11), p. 114309.
[17] Shaik, S., and van Hout, R., 2023, "Kinematics of Rigid Fibers in a Turbulent Channel Flow," Int. J. Multiphase Flow, **158**, p. 104262.
[18] Cui, Z., Qiu, J., Jiang, X., and Zhao, L., 2023, "Effect of Fluid Inertial Torque on the Rotational and Orientational Dynamics of Tiny Spheroidal Particles in Turbulent Channel Flow," J. Fluid Mech., **977**, p. A20.
[19] Sulaiman, M., Climent, E., Delmotte, B., Fede, P., Plouraboué, F., and Verhille, G., 2019, "Numerical Modelling of Long Flexible Fibers in Homogeneous Isotropic Turbulence," Eur. Phys. J. E, **42**(10), pp. 1–11.
[20] Oehmke, T. B., Bordoloi, A. D., Variano, E., and Verhille, G., 2021, "Spinning and Tumbling of Long Fibers in Isotropic Turbulence," Phys. Rev. Fluids, **6**(4), p. 044610.
[21] Rosti, M. E., Banaei, A. A., Brandt, L., and Mazzino, A., 2018, "Flexible Fiber Reveals the Two-Point Statistical Properties of Turbulence," Phys. Rev. Lett., **121**(4), p. 044501.
[22] Rosti, M. E., Olivieri, S., Banaei, A. A., Brandt, L., and Mazzino, A., 2020, "Flowing Fibers as a Proxy of Turbulence Statistics," Meccanica, **55**(2), pp. 357–370.
[23] Olivieri, S., Mazzino, A., and Rosti, M. E., 2021, "Universal Flapping States of Elastic Fibers in Modulated Turbulence," Phys. Fluids, **33**(7), p. 071704.
[24] Olivieri, S., Mazzino, A., and Rosti, M. E., 2022, "On the Fully Coupled Dynamics of Flexible Fibres Dispersed in Modulated Turbulence," J. Fluid Mech., **946**, p. A34.
[25] Andrić, J., Fredriksson, S. T., Lindström, S. B., Sasic, S., and Nilsson, H., 2013, "A Study of a Flexible Fiber Model and Its Behavior in DNS of Turbulent Channel Flow," Acta Mech., **224**(10), pp. 2359–2374.
[26] Dotto, D., and Marchioli, C., 2019, "Orientation, Distribution, and Deformation of Inertial Flexible Fibers in Turbulent Channel Flow," Acta Mech., **230**(2), pp. 597–621.
[27] Dotto, D., Soldati, A., and Marchioli, C., 2020, "Deformation of Flexible Fibers in Turbulent Channel Flow," Meccanica, **55**(2), pp. 343–356.
[28] Di Giusto, D., and Marchioli, C., 2022, "Turbulence Modulation by Slender Fibers," Fluids, **7**(8), p. 255.
[29] Brouzet, C., Verhille, G., and Le Gal, P., 2014, "Flexible Fiber in a Turbulent Flow: A Macroscopic Polymer," Phys. Rev. Lett., **112**(7), p. 074501.
[30] Bec, J., Brouzet, C., and Henry, C., 2024, "Enhanced Transport of Flexible Fibers by Pole Vaulting in Turbulent Wall-Bounded Flow," Phys. Rev. Fluids, **9**(6), p. L062501.
[31] Lindström, S. B., and Uesaka, T., 2007, "Simulation of the Motion of Flexible Fibers in Viscous Fluid Flow," Phys. Fluids, **19**(11), p. 113307.
[32] Cox, R., 1971, "The Motion of Long Slender Bodies in a Viscous Fluid. Part 2. Shear Flow," J. Fluid Mech., **45**(4), pp. 625–657.
[33] Kim, S., and Karrila, S. J., 2013, *Microhydrodynamics: Principles and Selected Applications*, Butterworth-Heinemann, Boston, MA.
[34] Guazzelli, E., and Pouliquen, O., 2018, "Rheology of Dense Granular Suspensions," J. Fluid Mech., **852**, p. P1.
[35] Canuto, C., Hussaini, M. Y., Quarteroni, A., and Zang, T. A., 2007, *Spectral Methods: Fundamentals in Single Domains*, Springer Science & Business Media, Berlin, Heidelberg.
[36] Moses, K. B., Advani, S. G., and Reinhardt, A., 2001, "Investigation of Fiber Motion Near Solid Boundaries in Simple Shear Flow," Rheol. Acta, **40**(3), pp. 296–306.
[37] Capone, A., Miozzi, M., and Romano, G. P., 2017, "On Translational and Rotational Relative Velocities of Fibers and Fluid in a Turbulent Channel Flow With a Backward-Facing Step," Int. J. Multiphase Flow, **94**, pp. 189–200.
[38] Alipour, M., De Paoli, M., and Soldati, A., 2022, "Influence of Reynolds Number on the Dynamics of Rigid, Slender and Non-Axisymmetric Fibres in Channel Flow Turbulence," J. Fluid Mech., **934**, p. A18.
[39] Baker, L. J., and Coletti, F., 2022, "Experimental Investigation of Inertial Fibres and Disks in a Turbulent Boundary Layer," J. Fluid Mech., **943**, p. A27.
[40] Byron, M., Einarsson, J., Gustavsson, K., Voth, G., Mehlig, B., and Variano, E., 2015, "Shape-Dependence of Particle Rotation in Isotropic Turbulence," Phys. Fluids, **27**(3), p. 035101.
[41] Parsa, S., and Voth, G. A., 2014, "Inertial Range Scaling in Rotations of Long Rods in Turbulence," Phys. Rev. Lett., **112**(2), p. 024501.
[42] Giurgiu, V., Caridi, G. C. A., De Paoli, M., and Soldati, A., 2024, "Full Rotational Dynamics of Plastic Microfibers in Turbulence," Phys. Rev. Lett., **133**(5), p. 054101.
[43] Sheikh, M. Z., Gustavsson, K., Lopez, D., Lévêque, E., Mehlig, B., Pumir, A., and Naso, A., 2020, "Importance of Fluid Inertia for the Orientation of Spheroids Settling in Turbulent Flow," J. Fluid Mech., **886**, p. A9.
[44] Olivieri, S., Brandt, L., Rosti, M. E., and Mazzino, A., 2020, "Dispersed Fibers Change the Classical Energy Budget of Turbulence Via Nonlocal Transfer," Phys. Rev. Lett., **125**(11), p. 114501.
[45] Di Giusto, D., Bergougnoux, L., Marchioli, C., and Guazzelli, E., 2024, "Influence of Small Inertia on Jeffery Orbits," J. Fluid Mech., **979**, p. A42.